EES Solar

PAPER

View Article Online
View Journal | View Issue

Cite this: *EES Sol.*, 2025, **1**, 1004

Interfacial reactions between atomic layer deposited NiO_x hole transport layers and metal halide perovskites in n-i-p perovskite solar cells

Nitin Mallik,[a] Javid Hajhemati,[a] Vincent Dufoulon,[a] Damien Coutancier,[a] Elif Hüsam,[b] Davide Regaldo,[cd] Iwan Zimmermann,[c] Karim Medjoubi,[c] Michael A. Anderson,[b] Damien Aureau,[e] Mathieu Frégnaux,[e] Roberto Félix,[b] Regan G. Wilks,[bf] Nathanaelle Schneider,[a] Marcus Bär[bfgh] and Philip Schulz *[a]

The hole transport layer (HTL) plays a critical role for the stability and efficiency of perovskite solar cells (PSCs) as it forms a direct interface with the metal halide perovskite (MHP) and contact electrode. In the widely researched n-i-p architecture PSCs, organic HTLs like p-doped spiro-OMeTAD (2,2′,7,7′-tetrakis[*N*,*N*-di(4-methoxyphenyl) amino]-9,9′-spirobifluorene) and PTAA (poly-[bis(4-phenyl)(2,4,6-trimethylphenyl)amine]) are commonly used to fabricate high-efficiency devices. Despite the high efficiency, the inherent instability and hygroscopic nature of these doped organic HTLs are of major concern for the stability of PSCs. In this work, we incorporated atomic layer deposition (ALD) based nickel oxide NiO_x HTLs into n-i-p PSCs, which serve the function of effective charge selective transport and pre-encapsulation layers and investigated its interface formation with the MHP using synchrotron-based hard X-ray photoelectron spectroscopy. Our study reveals that the ALD-NiO_x film grown on the MHP contained a high concentration of hydroxide and oxy-hydroxide species. Additionally, defect species, including nitrogen and lead-based compounds, formed in the perovskite layer at the interface, which adversely affected PSC performance. To mitigate undesirable chemical reactions that occur during the ALD process, we introduced a 20 nm PTAA interlayer as a buffer between the MHP and ALD-NiO_x layers. This resulted in improved device efficiency and enhanced operational stability.

Received 28th March 2025
Accepted 15th August 2025

DOI: 10.1039/d5el00044k

rsc.li/EESSolar

Broader context

Perovskite solar cells (PSCs) have demonstrated high efficiency but face stability challenges due to the instability of metal halide perovskites (MHP) absorbers, interlayers, and interfaces. The hole transport layer (HTL) is crucial for PSC stability and efficiency as it forms a direct interface with the MHP. Organic HTLs like spiro-OMeTAD and PTAA enable high efficiency but suffer from instability. Atomic layer deposition (ALD)-grown nickel oxide (NiO_x) is a stable alternative, but its interaction with MHP can introduce interfacial defects. Understanding ALD precursor interactions with MHP is key to developing a damage-free ALD process. Using synchrotron-based hard X-ray photoelectron spectroscopy (HAXPES), we investigated the top and buried interfaces between ALD-NiO_x and MHP in the n-i-p architecture. We identified hydroxide/oxy-hydroxide species in NiO_x and defect species, including nitrogen and lead compounds, at the MHP interface, negatively affecting PSC performance. To mitigate these reactions, we introduced a 20 nm PTAA buffer layer, improving efficiency and stability. This work provides insights into interface formation between ALD-grown metal oxides and MHPs. The use of an organic buffer layer as an interlayer design strategy highlights a promising approach to mitigate interfacial defects, paving the way for further optimization of stable and efficient PSCs.

[a]*Institut Photovoltaïque d'Île-de-France (IPVF), UMR 9006, CNRS, Ecole Polytechnique – IP Paris, Chimie Paristech – PSL, Palaiseau, 91120, France. E-mail: philip.schulz@cnrs.fr*

[b]*Dept. Interface Design, Helmholtz-Zentrum Berlin für Materialien und Energie GmbH (HZB), 12489, Berlin, Germany*

[c]*Institut Photovoltaïque d'Ile-de-France, 91120 Palaiseau, France*

[d]*Laboratoire de Génie Electrique et Electronique de Paris, Université Paris-Saclay, CentraleSupélec, CNRS, Gif-sur-Yvette, France*

[e]*Institut Lavoisier de Versailles, Université de Versailles Saint-Quentin-en-Yvelines, Université Paris-Saclay, CNRS, UMR 8180, Versailles Cedex 78035, France*

[f]*Energy Materials In Situ Laboratory Berlin (EMIL), HZB, 12489 Berlin, Germany*

[g]*Dept. X-ray Spectroscopy at Interfaces of Thin Films, Helmholtz-Institute Erlangen-Nürnberg for Renewable Energy (HI ERN), 12489 Berlin, Germany*

[h]*Dept. of Chemistry and Pharmacy, Friedrich-Alexander-Universität Erlangen-Nürnberg (FAU), 91058 Erlangen, Germany*

1. Introduction

In the last decade, hybrid organic inorganic metal halide perovskite (MHP) based solar cells have demonstrated rapid improvement in efficiency with the best power conversion efficiency (PCE) of 26.7% for a single junction solar cell and 33.9% for a perovskite-silicon two-terminal tandem cell.[1–3] This dramatic increase in perovskite solar cell (PSC) performance was due to exceptional optoelectronic properties of MHPs like outstanding light absorption ($\sim 10^4$ cm^{-1}), high photoluminescence quantum yields, tunable bandgaps (1.24–3.55 eV), narrow-band emission, and long diffusion lengths (~10–100 μm).[4] Furthermore, advancements in interface and

interlayer design between MHP and charge transport layers (CTLs) have played a crucial role in passivating the MHP surface, thereby contributing to improved PCE in PSCs.[5–8] However, the long-term stability issue of PSCs due to the instability of MHP materials, associated interlayers, and interfaces are major roadblocks for the commercialization of the perovskite technology.[9,10]

To date, the record efficiencies for single junction PSCs have been achieved using n-i-p architectures, which are commonly based on inorganic electron transport layers (ETLs) such as SnO_2 or TiO_2 and organic hole transport layers (HTLs) such as p-doped spiro-OMeTAD (2,2′,7,7′-tetrakis[*N*,*N*-di(4-methoxyphenyl)amino]-9,9′-spirobifluorene) and PTAA (poly-[bis(4-phenyl)(2,4,6-trimethylphenyl)amine]).[11,12] Despite the high PCE, the inherent instability of these doped organic HTLs is of major concern for the operational lifetime of PSCs. The dopants used in spiro-OMeTAD and PTAA are hygroscopic and can accelerate the degradation process.[13,14] Furthermore, under thermal stress, dopants such as 4-*tert* butylpyridine (*t*BP) can cause morphological deformation, *e.g.* the formation of pinholes due to its low boiling point.[15,16] The pinholes in the HTL enable ion migration processes between the dopant, MHP, and electrode ions.[17,18] In addition, minor deviations in the concentration of dopant and environmental conditions can significantly impact the conductivity of these organic HTLs, thereby affecting their reproducibility. Consequently, organic HTL-based n-i-p PSCs suffer from low operational stability despite the exceptionally high initial device efficiencies. Alternatively, inorganic metal oxides HTLs such as NiO_x, VO_x, and CuO_x could potentially improve PSCs stability due to their high resilience to heat, light, and moisture.[19] Furthermore, such dense inorganic layers can serve as effective barriers for ion migration and moisture ingress and hence function as an encapsulation film on the device level. Among the various metal oxides used in PSCs, NiO_x is the most researched and widely used owing to chemical stability and abundance.[20] The oxide layer possesses desirable properties such as a band gap greater than 3.6 eV, high transmittance in the near ultraviolet and visible regions, and excellent thermal, chemical, and light stability, making it a promising material for MHP technologies.[21] To date, deployment in devices has led to a maximum PCE of over 23% in p-i-n configuration.[22]

In this study, we employed atomic layer deposition (ALD) for the fabrication of NiO_x in n-i-p architecture PSCs. The ALD technique is promising for growing metal oxide layers for application in PSCs due to its relatively low deposition temperature (room temperature), uniform coverage, and industrial scalability.[23] Using the ALD process, a dense ultrathin metal oxide film could be deposited that can act as encapsulation to the outer environment and block internal ion migration in PSCs.[24] However, the direct application of ALD on MHPs presents significant challenges due to the inherent reactivity of halide anions and organic cations (*e.g.*, methylammonium MA^+, formamidinium FA^+) at the MHP surface.[25,26]

The successful integration of ALD-grown metal oxides on top of MHPs surface depends on three fundamental parameters: (i) process conditions (temperature and pressure), (ii) oxidant precursor chemistry, and (iii) metal precursor chemistry. Studies have shown that mixed-cation CsFA MHP generally maintains good stability at temperatures up to 100 °C under vacuum conditions in comparison to $MAPbI_3$.[23,27,28] This is particularly relevant for ALD processes, which are commonly performed under vacuum, although atmospheric-pressure ALD also exists. Our previous study demonstrated that $FA_{0.7}Cs_{0.3}Pb(I_{0.9}Br_{0.1})_3$ MHP maintained bulk structural stability after 1 hour of heat treatment under simulated operational ALD conditions (1–3 mbar, N_2, 100 °C).[28] Similarly, Bracesco *et al.* reported negligible changes in $Cs_{0.15}FA_{0.85}Pb(I_{0.92}Br_{0.08})_3$ based MHP exposed to 100 °C for 90 minutes under high vacuum (10^{-5} mbar), as observed by *in situ* IR spectroscopy.[27]

The choice of oxidant precursors plays a critical role in determining reaction outcomes, depending on the composition of the MHP. Ozone (O_3) induces universal degradation of MHPs due to its highly oxidative nature,[29] while water (H_2O) exhibits composition-dependent behavior,[30,31] degrading $MAPbI_3$ even at room temperature[32] but preserving CsFA based MHP systems.[33–35] Hydrogen peroxide (H_2O_2) has emerged as a promising alternative, enabling the deposition of ALD-grown metal oxides (such as SnO_2) with low oxygen vacancy concentrations, leading to improved charge transport properties[36] while causing no observable damage to CsFA-based MHPs.[28]

Nevertheless, organometallic precursor chemistry remains the dominant factor in interfacial degradation of MHP. Alkyl-metal precursors like diethylzinc lead to perovskite decomposition *via* proton transfer,[37] while amino-based precursors such as tetrakis(dimethylamido)tin (TDMASn) generate nanoscale interfacial defects.[26,38,39] Our previous work using X-ray photoelectron spectroscopy revealed that TDMASn produces a defective interface layer containing *sym*-triazine (N 1s = 398.7 eV) and PbI_2, creating a 400 meV electron transport barrier in $FA_{0.7}Cs_{0.3}Pb(I_{0.9}Br_{0.1})_3/SnO_2$ heterostructures with detrimental impact on PSCs performance.[28]

Building on this fundamental understanding, we investigate ALD-NiO_x as an alternative to organic HTLs in n-i-p architecture solar cells, focusing on its potential for high-stability PSCs. The primary focus of this study is to comprehensively investigate the interface between $FA_{0.7}Cs_{0.3}Pb(I_{0.9}Br_{0.1})_3$ MHP and ALD-NiO_x using synchrotron-based hard X-ray photoelectron spectroscopy (HAXPES). The aim of our investigation is to understand the chemical interaction between the ALD-NiO_x precursors and the MHP, the interface formation between the two material systems, and the impact on PSC performance. Additionally, we introduce a PTAA organic buffer layer between MHP and ALD-NiO_x to enable a comparative analysis and mitigate potential interfacial reactions between the MHP and ALD-NiO_x. Furthermore, we assess the operational stability of the ALD-NiO_x-based n-i-p PSCs.

2. Results and discussion

The half-cell device architectures used in this study are comprised of a fluorine doped tin oxide(FTO)-coated glass substrate, a 10 nm thick SnO_2 electron transport layer, a 400 nm thick double cation MHP layer with the composition $FA_{0.7}Cs_{0.3}Pb(I_{0.9}Br_{0.1})_3$ with and without a 20 nm thick buffer layer of PTAA, and finally the NiO_x layer (62 ALD cycles) as shown in

Fig. 1(a). The deposition of 62 ALD cycles of NiO_x yields a 5 nm thick film on a reference silicon substrate, as determined by ellipsometry (see SI Section 2, Fig. S2). However, since ALD is a substrate-dependent technique, the actual film thickness may vary across different substrates due to variations in surface chemical properties. For instance, the thickness of the NiO_x overlayer grown on MHP and PTAA was estimated using the attenuation of HAXPES core-level signals induced by the NiO_x film. Under identical conditions of 62 ALD cycles, the estimated thicknesses are 3.9 nm on MHP and 1.4 nm on PTAA (details provided in SI, Section 7, Table S7). In this report, we denote the number of ALD cycles rather than the resulting film thickness.

In Fig. 1(b) we show the X-ray diffraction (XRD) patterns of the bare MHP film and the MHP with ALD-NiO_x, PTAA, and PTAA/ALD-NiO_x overlayers. The XRD signature with 2θ in the range of 12–15° displays signals corresponding to the (110) plane of the MHP (see SI, Section 3, Fig. S4 for XRD pattern in the range of 10–50°). The XRD signature of the MHP material did not exhibit any change for the samples with the ALD-NiO_x overlayer in comparison with the reference MHP and MHP/PTAA samples. Typically, any unwanted reaction between ALD precursors and MHP is expected to result in the evolution of an XRD peak at approximately 12.5°, which is indicative of the formation of (poly)crystalline PbI_2 as a result of MHP degradation.[28] However, in this particular case with the ALD-NiO_x overlayer, we did not observe any formation of such compounds. This implies that the bulk structure of the MHP material remained unchanged after exposure to the ALD-NiO_x conditions (precursors, 1–2 mbar pressure level, temperature of 100 °C), *i.e.*, any potential degradation reaction thus occurs in only a very limited region of the formed interface (and thus is beyond the bulk sensitivity of XRD) or results in amorphous compounds. This exceptional bulk stability can be attributed to the inherent compositional robustness of the $FA_{0.7}Cs_{0.3}Pb(I_{0.9}Br_{0.1})_3$ MHP used in this study. Although perovskite materials are generally known to degrade upon exposure to moisture or water-based environments, our CsFA-based composition exhibits high resilience even when directly exposed to H_2O during the ALD metal oxide growth process. In particular, the presence of FA^+ cation enhances hydrophobicity and reduces water uptake compared to MA^+ cation based MHP,[40,41] while partial substitution with cesium cation (Cs^+) induces lattice contraction that increases the hydration activation barrier to ~0.53 eV,[42] thereby kinetically suppressing water-induced degradation. In addition, bromide alloying mitigates halide segregation,[43] further contributing to the enhanced resistance to moisture and thermal stress. These compositional attributes, combined with the relatively mild ALD conditions (limited ALD precursors pulse time, see SI, Section 1.2), explain the preservation of the bulk crystalline structure, consistent with our experimental findings in Fig. 1(b).

We now turn to the evolution of the MHP/ALD-NiO_x interface chemistry before and after NiO_x deposition as investigated using synchrotron-based HAXPES. The measurements were conducted at the HiKE end station at the BESSY II KMC-1 beamline at the Helmholtz-Zentrum Berlin für Materialien und Energie GmbH (HZB)[44,45] using photon energies of 2 keV and 6 keV to probe the top region and deeper buried interface region, respectively. For instance, the I 3d core level signal of the pristine MHP sample is detected from a maximum depth of ~10 nm with 2 keV photon energy and ~25 nm with 6 keV photon energy, corresponding to approximately three times the photoelectron inelastic mean free path (see SI, Table S1 for IMFP values and Section 2 for discussion on surface roughness and its relevance to differentiating surface and subsurface contributions). We employ the same detailed HAXPES characterization methodology and data treatment parameters as reported previously (see SI, Section 1.4).[28]

The HAXPES spectra of the I $3d_{5/2}$, N 1s, and Pb 4f core level regions from the bare MHP samples and the MHP samples after ALD-NiO_x deposition are depicted in Fig. 2. The intensities of the MHP core levels are normalized to the maximum intensity

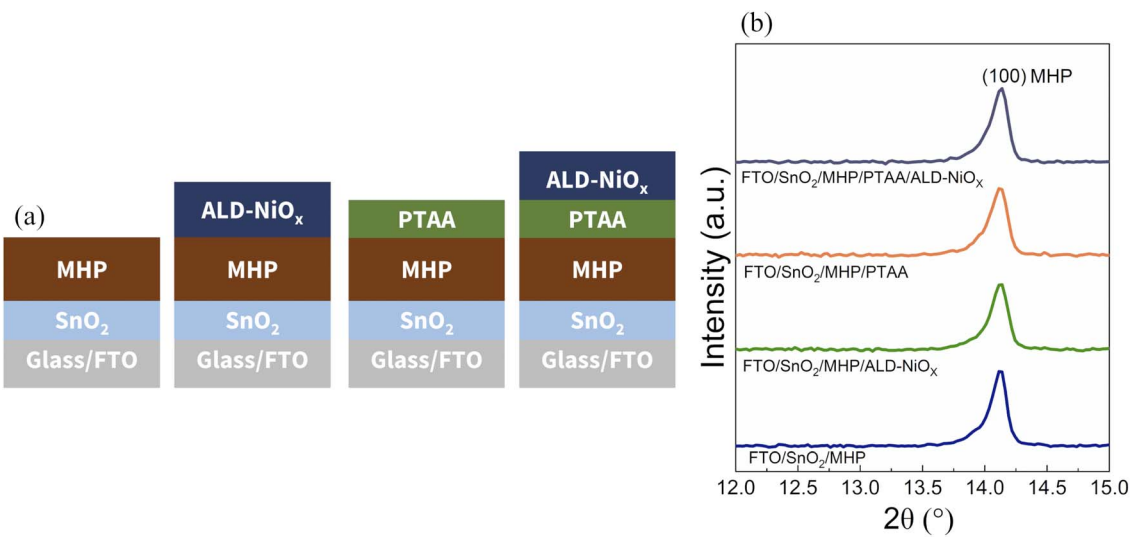

Fig. 1 (a) Schematic of the different device architectures used in this section for interface study, (b) XRD patterns of MHP film with and without ALD-NiO_x, PTAA, PTAA/ALD-NiO_x top layers.

for improved data visualization and interpretation. The I $3d_{5/2}$ and Pb 4f core level signals of the pristine MHP show a minor shift in peak position of 100 meV towards higher binding energy between the data acquired with photon energies of 2 keV and 6 keV, respectively (see SI, Table S3). We consider a shift of this order of magnitude borderline in terms of significance, as the spectral resolution of our HAXPES experiment is in a similar range. In any case, if present at all an (upward) band bending at the bare MHP surface that would explain this shift would be small.

After NiO_x deposition on the MHP, we do not observe any significant change in peak position for the I $3d_{5/2}$ core level at both 2 keV and 6 keV photon energies with respect to the bare MHP film (Fig. 2(a), (d), and SI, Table S3). At the same time, the full-width-at-half-maximum (FWHM) value of the I $3d_{5/2}$ peak increases by 100 meV from 1.0 eV for the bare MHP surface to 1.1 eV for the MHP film after NiO_x deposition (for both 2 keV and 6 keV measurements). In contrast to these observations in the iodine core levels, the Pb 4f core level shifts to higher binding energy by 200 meV, *i.e.* from 138.6 eV to 138.8 eV for Pb $4f_{7/2}$ at 2 keV photon energy, after NiO_x deposition. However, the Pb $4f_{7/2}$ peak remains at 138.6 eV at 6 keV photon energy for both samples with and without NiO_x overlayer, indicating that this change is confined to the interface region (see Fig. 2(c) and (f))). Additionally, we observe the FWHM value of the Pb $4f_{7/2}$ peak increasing from 0.7 eV for the bare MHP surface at both photon energies, to 1.0 eV and 0.9 eV for the sample with the NiO_x overlayer at 2 keV and 6 keV photon energies, respectively. The core level shift and peak broadening at 2 keV originate from top interface Pb atoms, likely due to the formation of a small fraction of interfacial Pb–O–Ni bonds.[46] The absence of a shift and reduced broadening at 6 keV where the signal originates from deeper regions in the MHP confirms that these chemical interactions are confined to the top interface region.

In addition, we determined the ratio of iodine to lead in the top region (2 keV) and buried (interface) region (6 keV) of the MHP layer before and after ALD-NiO_x deposition. The quantifications reveal that before NiO_x deposition, the I/Pb ratio near the MHP surface (measured using 2 keV) is 2.8 ± 0.1, which is close to the expected stoichiometric value of 2.7. The I/Pb ratio in the MHP subsurface (measured using 6 keV) is 2.4 ± 0.1, indicating a slight iodine deficiency in the deeper region of the MHP. After NiO_x deposition, we observe a more severe iodine deficiency. The I/Pb ratio decreases to 1.6 ± 0.1 and 1.9 ± 0.1 using 2 keV and 6 keV photon energy, respectively. This suggests that the reduction in iodine content is more pronounced at the interface between the MHP film, and the ALD layer likely driven by unwanted chemical interactions of the MHP with the ALD-NiO_x or the ALD precursors during NiO_x deposition. The performance of PSCs can be severely impacted by deep-level defects caused by halide deficiency, which may hinder charge carrier extraction.[47]

The N 1s core level spectra of the reference MHP film (Fig. 2(e), blue spectra) exhibited a peak corresponding to the FA species (N_{FA}) at binding energies of 400.8 eV (2 keV) and 401.0 eV (6 keV). Following NiO_x deposition, this peak shifted by 100 meV toward lower binding energies at both photon energies (Fig. 2(e), green spectra), but since the shift falls within the experimental resolution, it is not considered significant. Following NiO_x deposition, the N 1s signal exhibited increased noise (Fig. 2(b)), likely due to signal attenuation by the NiO_x overlayer and potential nitrogen loss during the ALD process. In contrast, the 6 keV data (Fig. 2(e)) appear less noisy, attributed to reduced attenuation at higher photon energies. Additionally, two new nitrogen components, denoted N^1 and N^2, emerged at lower binding energies in the N 1s core-level spectra after NiO_x deposition. The N^1 species (~400.0 eV peak) may originate from neutral amidinate nitrogen (δ^0) or from nitrogen species such as imine, amine, or pyrrolic N formed through partial decomposition of the FA cation or interfacial reactions with the Ni precursor.[48,49] In contrast, the N^2 peak (~398.8 eV) is consistent with negatively charged amidinate nitrogen (δ^-) coordinated to Ni or Ni–N bonding environments derived from residual $Ni(amd)_2$ precursors.[49] The coexistence of such species indicates complex interfacial chemistry that can hinder charge transport, severely impacting device performance. While the exact molecular identity of these nitrogen species cannot be unambiguously determined by XPS alone due to overlapping binding energies and interfacial complexity, the data clearly indicate the formation of nitrogen-related interfacial defects induced by the ALD process.

Moreover, the intensity of the additional nitrogen ($N^1 + N^2$) peaks decreased with increasing photon energy (2 → 6 keV), resulting in a decreased $(N^1 + N^2)/N_{FA}$ ratio (1.30 → 0.75), suggests that these nitrogen-based defect species are predominantly localized within the top interfacial region of the MHP. The depth sensitivity is related to the lower inelastic mean free path of the ~1.6 keV photoelectrons (*i.e.*, from N 1s core levels excited with 2 keV X-rays) than of the ~5.6 keV photoelectrons (from N 1s core levels excited with 6 keV X-rays).

Furthermore, we determined the N_{FA} to Pb ratio before and after the ALD process using both 2 and 6 keV measurements. We found a significant loss of N_{FA}, with the N_{FA}/Pb ratio decreased from 0.82 to 0.37 at 2 keV and from 0.72 to 0.47 at 6 keV. In addition to the previously observed iodine loss, these results confirm that the MHP becomes deficient in both nitrogen and iodine after the ALD process. This combined deficiency is consistent with a redox reaction occurring at the perovskite/NiO_x interface during the initial ALD process. This behavior aligns with observations by Boyd *et al.*, who reported that interactions between NiO_x surfaces and perovskite can lead to the loss of FA^+ and I^- species, resulting in a cation-deficient MHP.[50] The more pronounced loss of both N_{FA} and iodine at 2 keV photon energy, compared to 6 keV, confirms that the redox reactions are primarily localized to the top MHP interface. Such material loss from the perovskite structure inevitably contributes to interfacial degradation and can compromise device stability. Despite the observed loss of N_{FA} from the MHP due to the interfacial reaction, we additionally observed an increase in the N_{total} $(N_{FA} + N^1 + N^2)$/Pb ratio for MHP/NiO_x compared to the N_{FA}/Pb ratio of the pristine MHP sample, which increased from 0.82 to 0.86 at 2 keV and from 0.72 to 0.82 at 6 keV photon energies. This quantitative increase in total nitrogen content, primarily from the contribution of N^1 and N^2 species despite the

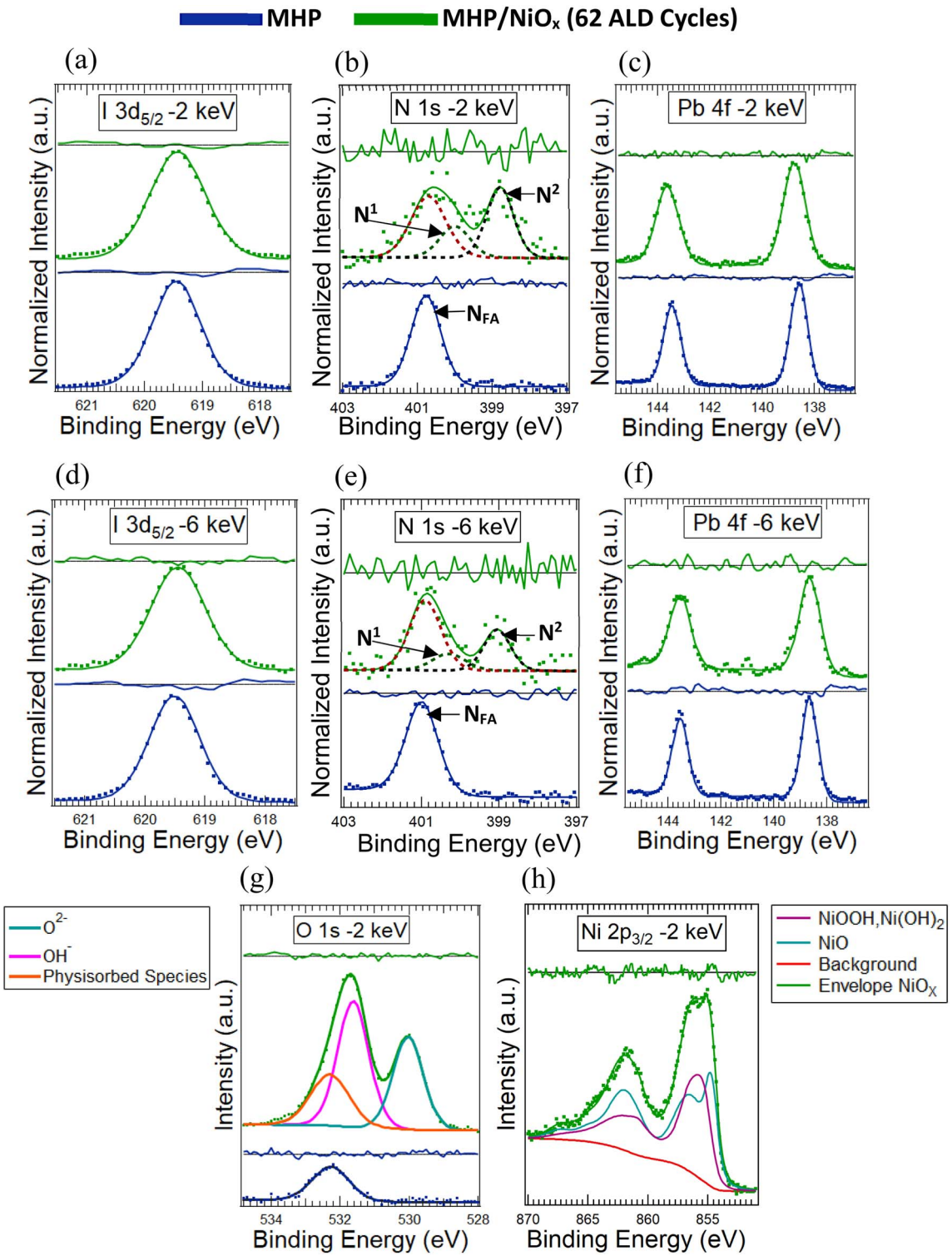

Fig. 2 (a–h) HAXPES detail spectra (including fits and residua) of the (a and d) I $3d_{5/2}$, (b and e) N 1s, (c and f) Pb 4f, (g) O 1s, and (h) Ni $2p_{3/2}$ core levels of MHP without (blue spectra) and with (green spectra) 62 ALD cycle NiO_x top layers recorded with (a–c, g and h) 2 keV and (d–f) 6 keV photon energies.

loss of N_{FA}, reconfirms the likely presence of residual fragments of the bis(*N*,*N*′-di-*tert*-butylacetamidinato)nickel(II) $Ni(amd)_2$ precursor and/or trapped species formed *via* FA decomposition or chemical interaction with the Ni precursor.

In order to determine whether the defect interface species is formed because of interaction with the ALD-NiO_x during interface formation or with the ALD precursors [H_2O and $(Ni(amd)_2)$] in the initial phase of the NiO_x deposition, additional lab-based

X-ray photoelectron spectroscopy (XPS) (Al K_α, 1486.7 eV) measurements of Si, MHP, and MHP/PTAA samples exposed to the to the ALD-NiO_x precursors $Ni(amd)_2$ or H_2O were performed; the corresponding N 1s core level spectra are shown in Fig. 3. The N 1s peak originating from the $Ni(amd)_2$ component is located at 401 eV on the silicon sample, as shown in Fig. 3(a). In addition, we observed a low-intensity nitrogen peak ($N_{by\text{-}product}$) at a binding energy of 399.3 eV (Fig. 3(a)), which we suspect is a by-product of the $Ni(amd)_2$ precursor caused by short-term air exposure during sample transfer.

In Fig. 3(b), the N 1s core level spectra of the MHP sample (N_{FA} peak at 401 eV) shows no changes after exposure to 62 pulses of the H_2O precursor (green) compared to the reference MHP sample (red). However, upon exposure to 62 pulses of the $Ni(amd)_2$ precursor (blue, Fig. 3(b)), two additional peaks emerge at binding energies of 400 eV and 399.2 eV, corresponding to the N^1 and N^2 components. These secondary N 1s features are consistent with those observed in the NiO_x/MHP sample (Fig. 2). Notably, the $(N^1 + N^2)/N_{FA}$ ratio in this case is ~0.61 for MHP/$Ni(amd)_2$, significantly lower than the value of 1.30 observed for the MHP/NiO_x sample at 2 keV. This difference arises because, in the current measurement, the $Ni(amd)_2$ precursor forms only a thin chemically bound layer, allowing detection of photoelectrons from deeper within the MHP (~7 nm, with lab XPS 1486.7 eV), whereas in the NiO_x/MHP case, the 3.9 nm NiO_x overlayer attenuates the N_{FA} signal, limiting the probed depth to the top ~1–2 nm (with 2 keV HAXPES) of the MHP. Taken together, these spectral changes clearly indicate that while the MHP surface remains chemically stable under ALD conditions involving H_2O exposure at 100 °C and a vacuum of 1–3 mbar, it reacts notably with the $Ni(amd)_2$ precursor. The appearance of additional nitrogen species suggests that the MHP is susceptible to metallic precursor induced interfacial degradation, leading to the formation of chemical defects. These findings confirm that interfacial degradation in MHP during ALD is primarily driven by the $Ni(amd)_2$ precursor, rather than by thermal effects, vacuum conditions, or exposure to H_2O.

Next, to reveal the chemical structure of the ALD deposited NiO_x film, we focus on the Ni $2p_{3/2}$ and O 1s core levels, as shown in Fig. 2(g and h). NiO_x films commonly exhibit multiple subspecies of the general formula NiO_xH_y, including NiO, $Ni(OH)_2$, NiOOH, and metallic nickel.[51,52] These subspecies, specifically $Ni(OH)_2$ and NiOOH, can exist in different phases, including, β-$Ni(OH)_2$, α-$Ni(OH)_2$, β-NiOOH, and γ-NiOOH.[53–56] It is important to note that the 6 keV data for the Ni $2p_{3/2}$ and O 1s core levels are excluded from this analysis due to the larger fitting error [see SI, Fig. S11 (standard deviation in the Ni $2p_{3/2}$ fitting) and Fig. S9 (6 keV plots)]. The O 1s core-level region contains three distinct contributions corresponding to O^{2-}, OH^-, and physisorbed species.[57,58] The O^{2-} contribution to the O 1s peak is located at a binding energy value of 530 eV when using 2 keV excitation (Fig. 2(g)), which we attribute to the NiO species in the NiO_x film. In addition, the O 1s peak positioned at 531.7 eV, is ascribed to the $Ni(OH)_2$ and/or NiOOH contribution in the NiO_x film. The O 1s core level component that arises from physisorbed (and thus less ordered) species is positioned at higher binding energies of 532.6 eV (for which we allow a slightly broader peak shape caused by slightly different binding energies for the different bond angles and distances in this presumably less ordered material). Upon qualitative comparison of OH^- and O^{2-} contributions, we find that there is a higher concentration of OH^- species in the NiO_x film. Of note, the O 1s core level is only qualitatively assessed here as there could be contributions from adventitious species overlapping with the main components related to ALD-NiO_x.[59]

We focus on the quantitative analysis on the Ni $2p_{3/2}$ peak for an estimation of the various contributions of Ni species in the

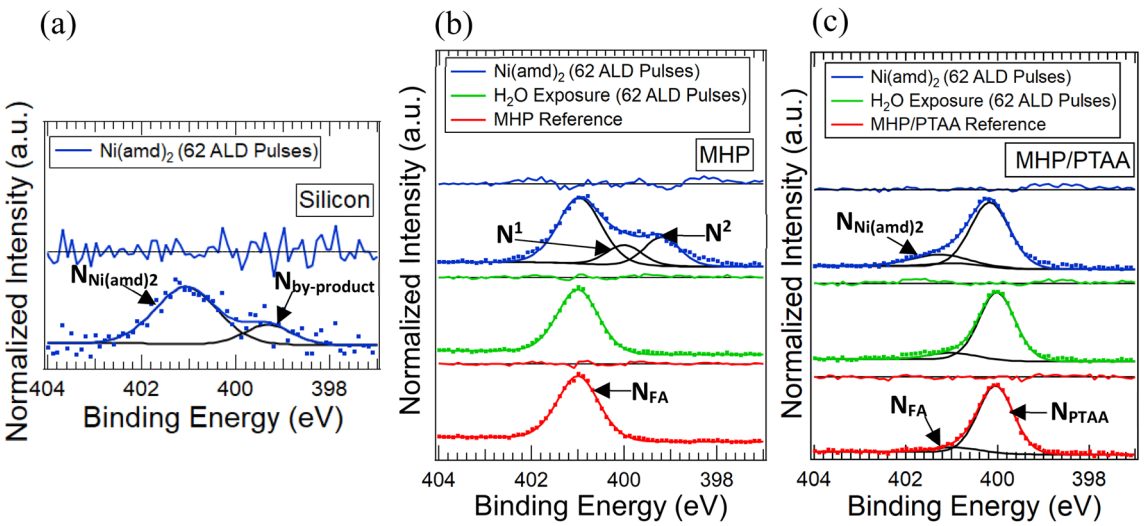

Fig. 3 XPS spectra (Al K_α, 1486.7 eV) of the N 1s core level of (a) a silicon wafer that has been exposed to the ALD-NiO_x precursor $Ni(amd)_2$, (b) an as-received MHP (reference) and MHP samples that have been exposed to 62 pulses of the ALD-NiO_x precursor bis(*N*,*N*′-di-*tert*-butylacetamidinato)nickel(II) $Ni(amd)_2$, or of H_2O, (c) an as-received MHP/PTAA (reference) and MHP/PTAA samples that have been exposed to 62 pulses of the ALD-NiO_x precursor $Ni(amd)_2$ or H_2O.

NiO_x film. The Ni $2p_{3/2}$ signal envelope was analyzed using the method developed by Biesinger *et al.*,[51] from which the Ni $2p_{3/2}$ signal from various NiO_xH_y subspecies was decomposed into their theoretical shake-up structure calculated by Gupta and Sen.[60,61] This particular procedure is based on the identification of 34 distinct peaks including the shake-up structures, each corresponding to one of the four primary chemical states of NiO_xH_y as described above. We decomposed the Ni $2p_{3/2}$ signal obtained from our samples based on the assumption that it would be a linear combination of individual signals from NiO, $Ni(OH)_2$, β-NiOOH, γ-NiOOH and metallic nickel with varying multiplet spacing. However, it is important to note that this assumption does not guarantee that the shake-up and plasmon loss structures for each phase in our samples mirror those of pure individual samples. Inelastic processes could potentially occur between photoelectrons and other atoms or molecules within the NiO_x structure,[62] impacting the HAXPES signal, and these factors were not considered in our analysis.

The Ni $2p_{3/2}$ core level is shown in Fig. 2(h) which displays the envelope for each subspecies of NiO_x, encompassing NiO, $Ni(OH)_2$/NiOOH and Ni metal (see SI, Fig. S8(a) for the original fitting) measured at 2 keV photon energy. Upon quantification, we found that the NiO contribution is 56%, while the combined concentration of $Ni(OH)_2$ and/or NiOOH accounts for the remaining 44%, with no traces of metallic Ni detected in the MHP/ALD-NiO_x film. In comparison, the ALD-NiO_x grown on a silicon wafer measured using lab based XPS (1486.7 eV) is found to be composed of 83% of NiO and 17% of $Ni(OH)_2$ and/or NiOOH species, respectively (see SI, Section 5 for detailed analysis and interpretation). The significant difference in the composition of ALD-NiO_x highlights the crucial role of surface termination of the substrates. Additionally, the high concentration of these –OOH species in NiO_x grown on the MHP surface can readily react with the halides present in the MHP, causing deterioration of the MHP film and the formation of numerous trap defects at the MHP/NiO_x interface.[50]

Next, we introduced a 20 nm PTAA buffer layer between the MHP and ALD-NiO_x to potentially mitigate interfacial defect formation during the ALD process. The interface chemistry is similarly studied using HAXPES photon energies of 2 keV and 6 keV and MHP peaks were detected at both photon energies as shown in Fig. 4. Detecting a signal from the buried MHP layer underneath the 20 nm thick PTAA layer, as shown in Fig. 4, is not expected for measurements pursued at 2 keV photon energy. This corresponds to a photoelectron inelastic mean free path 4–5 nm (see SI, Table S1), yielding an information depth of roughly 12–15 nm. Thus, our observation suggests the presence of pinholes in the PTAA layer, which is confirmed by corresponding scanning electron microscopy images (see SI, Section 4, Fig. S5(c)). The Pb 4f and I $3d_{5/2}$ core level peak positions, originating from the MHP signal, appear at slightly lower binding energies, shifted by 100 meV compared to the core levels measured for the bare MHP surface, though this minor shift falls within the experimental resolution.

After ALD-NiO_x deposition, the I $3d_{5/2}$ core level shifted by 200 meV to higher binding energy from 619.3 to 619.5 eV at 2 keV for the samples with MHP/PTAA and MHP/PTAA/NiO_x stacks, respectively (see SI, Table S6). However, we did not observe any shift in the I $3d_{5/2}$ core level core level binding energy at 6 keV excitations energy. The Pb 4f core level also shifted to a higher binding energy by 100 meV at both photon energies, 2 keV and 6 keV (see Fig. 4(c) and (f)). We do not consider this shift significant, as it falls within the spectral resolution of our HAXPES experiment, as discussed earlier in this article, and there is significant noise in these particular spectra.

Notably, the N 1s core level peak corresponding to the triaryl amine compound in PTAA shifted after the NiO_x deposition to a higher binding energy by 300 meV at both 2 keV and 6 keV excitations (see Fig. 4(e) and (e)), but the N_{FA} peak binding energy remained constant. The shift in the N 1s core-level peak associated with PTAA may arise from either the grafting of ALD-NiO_x onto the PTAA surface or the impact of the ALD process itself. Additionally, the unchanged binding energy position of the N_{FA} contribution to the N 1s core level after the ALD process indicates that the PTAA interlayer effectively suppresses unwanted chemical reactions between MHP and ALD-NiO_x precursors. However, there remains a possibility of unwanted chemical interactions occurring through pinholes in the PTAA film.

Next, we performed a quantitative analysis by estimating I/Pb for 2 keV and 6 keV measurements of the MHP film in the MHP/PTAA sample before and after ALD-NiO_x deposition. The quantification shows that before NiO_x deposition, the I/Pb ratios near the MHP surface (measured using 2 keV) and subsurface (measured using 6 keV) are 2.5 ± 0.1 and 2.7 ± 0.1, respectively. After NiO_x deposition, we observed a slight iodine deficiency with the I/Pb ratio dropping to 2.1 ± 0.1 and 2.4 ± 0.1 under 2 keV and 6 keV excitation energies respectively. This could be linked to the interaction of the ALD precursors with MHP through the pinholes, as hypothesized earlier in accordance with the binding energy shifts, but the effect is significantly attenuated compared to the values obtained for the MHP/ALD-NiO_x sample without PTAA interlayer. When comparing the change in the I/Pb ratio after the ALD-NiO_x process for MHP (~33% iodine loss) and MHP/PTAA (~12% iodine loss) samples, we observed that iodine loss is reduced significantly by the introduction of the PTAA buffer layer. The greater iodine retention highlights the effectiveness of the PTAA buffer layer in limiting the unwanted chemical interaction between MHP and ALD-NiO_x.

In addition, we exposed the MHP/PTAA sample to the individual ALD precursors (*i.e.*, H_2O and $Ni(amd)_2$) and tracked the N 1s core level using lab-based XPS (Al K_α, 1486.7 eV). We did not observe any change in the N 1s core level due to exposure to H_2O, as compared to the reference sample, with the peak positioned at 400 eV corresponding to the amine group in PTAA, as shown in Fig. 3(c). Upon exposure to the $Ni(amd)_2$ precursor, we observed the formation of a new peak at 400.9 eV, which is at the same peak position as the nitrogen contribution from the $Ni(amd)_2$ precursor itself (see Fig. 3(a)). This indicates successful chemical grafting of the $Ni(amd)_2$ precursor onto the PTAA surface. Moreover, we did not find any observable evidence of the formation of defect species in the MHP/PTAA

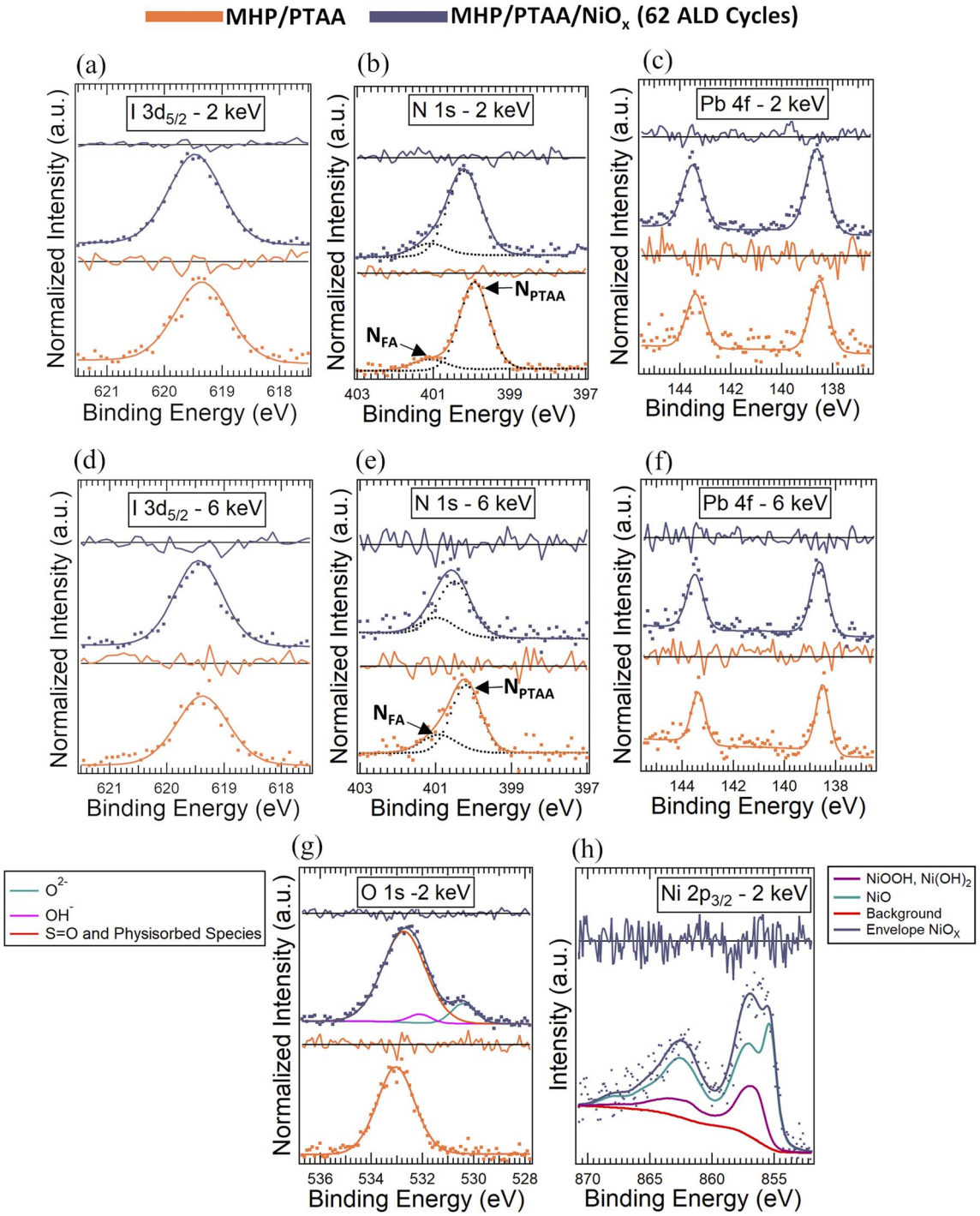

Fig. 4 (a–h) HAXPES detail spectra (including fits and residua) of I $3d_{5/2}$, N 1s, Pb 4f, O 1s, Ni $2p_{3/2}$ of MHP: PTAA without (orange spectra) and with (purple spectra) ALD-NiO_x top layers recorded with 2 keV and 6 keV excitation energy.

sample compared to the MHP sample, which suggests that PTAA film mitigates the interaction between the MHP film and the ALD precursors. However, the pinholes in the PTAA film remain of concern and likely have a detrimental impact on the performance or reproducibility of PSCs.

Upon inspecting the NiO_x core levels for the MHP/PTAA sample, the signal acquired at 6 keV for the Ni 2p and O 1s core levels exhibit a low signal-to-noise ratio due to the significantly thinner NiO_x layer compared to that of the PTAA-free MHP/NiO_x interface (see Discussion in SI, Section 7, Table S7), preventing us from incorporating this dataset into our quantitative analysis (see SI, Fig. S10). Hence, the photoemission spectroscopy examination of the NiO_x overlayer is limited to a photon energy of 2 keV. The O 1s spectra in Fig. 4(g), obtained from the MHP/PTAA sample at 2 keV, displays a peak positioned at 533 eV corresponding to both oxygen species

within the lithium bis(trifluoromethanesulfonyl)imide (LiTFSI) dopant of PTAA (refer to the F 1s core level in the survey spectra, which confirms LiTFSI doping in SI; Fig. S7) as well as physisorbed environmental species. Furthermore, after the NiO_x deposition, the spectra showed the emergence of two peaks at 530.4 eV and 532.1 eV, attributed to O^{2-} (NiO) and OH^- (hydroxide, oxy-hydroxide) species (see also Fig. 2(g)), respectively. This noticeable difference in intensity between the O^{2-} species and the OH^- species strongly suggests a significant contribution of NiO within the ALD film. As shown in Fig. 4(h), the Ni $2p_{3/2}$ core level components were found to be NiO, $Ni(OH)_2$/NiOOH with no indication of metallic nickel (see SI, Fig. S8(b) for the original fitting). Through quantitative analysis, we determined the composition to be 74% NiO, 26% $Ni(OH)_2$ and/or NiOOH (see SI, Fig. S11). In comparison to the NiO_x grown on MHP, we find a higher concentration of NiO in ALD-NiO_x film grown on the PTAA layer.

In addition, we analyzed the work function of ALD-NiO_x grown on MHP and PTAA by Kelvin probe measurements performed in nitrogen atmosphere. We find the work function of ALD-NiO_x on MHP to be 4.1 ± 0.1 eV (consistent with ultraviolet photoelectron spectroscopy results; see SI, Fig. S12), which is lower than that of the bare MHP surface (4.4 ± 0.1 eV). However, in comparison, the NiO_x grown on the MHP/PTAA film exhibited a higher work function of 4.5 ± 0.1 eV. We assume that the difference in the work function of NiO_x on MHP and PTAA is linked to the different stoichiometry of the ALD-NiO_x film as revealed in the HAXPES measurements. The NiO_x film grown on MHP consists of a high concentration of hydroxide and oxy-hydroxide species, that could lead to a low work function value,[63] which we suspect to be unsuitable for efficient hole extraction.

We now turn to the evaluation of the interlayer functionality in full device stacks. The current density–voltage (J–V) measurements of completed n-i-p perovskite solar cells with and without interlayer were carried out under standard conditions (AM 1.5G), as presented in Fig. 5(a) (see SI, Section 8 for statistical J–V data). We used the following cell configurations for this part of the study:

(a) Glass/FTO/SnO_2/MHP/PTAA/Au

(b) Glass/FTO/SnO_2/MHP/ALD-NiO_x/Au (see SI, Fig. S14)

(c) Glass/FTO/SnO_2/MHP/PTAA/ALD-NiO_x/Au

With the same deposition procedures as in the previous analysis with an active area of 0.09 cm^2. The Au contacts are 100 nm thick and were deposited by thermal evaporation directly on top of the HTL. Among these configurations, the reference devices utilizing PTAA as the HTL (configuration (a)) displayed optimal performance, reaching a maximum PCE of 10.5%, open-circuit voltage (V_{OC}) of 1.04 V, short-circuit current density (J_{SC}) of 18.1 mA cm^{-2} and fill factor (FF) of 56%. The relatively low PCE of PTAA-based PSCs is due to pinholes in the PTAA layer, which create direct contact between the metal electrode and the MHP layer. This bypasses the selective hole extraction function of the HTL, leading to increased non-radiative recombination (lowering V_{OC}) and the formation of shunt pathways (reducing FF).[64,65]

In contrast, the devices employing only the ALD-NiO_x as HTL (configuration (b)) were not functional (see SI, Fig. S14), confirming that the interfacial defects and a high concentration of hydroxyl-terminated NiO_x lead to device failure. Intriguingly, the devices that synergistically integrated PTAA and NiO_x bilayers (configuration (c)) exhibit significantly improved performance, with PCE values reaching as high as 17.5%, a V_{OC} of 1.13 V, J_{SC} of 21.5 mA cm^{-2}, and a fill factor of 72%. Furthermore, the external quantum efficiency (EQE) spectra of the PTAA/NiO_x HTL devices in Fig. 5(b) (in blue) demonstrated higher EQE in the range of 350–750 nm compared to the PTAA device (in orange).The incorporation of PTAA and ALD-NiO_x as a bilayer HTL led to a significant performance enhancement, achieving an efficiency of 17.5%, compared to 10.5% with PTAA as the sole HTL in our n-i-p PSCs. The protective role of the PTAA buffer layer during the ALD process, coupled with the efficient electron-blocking attributes of the NiO_x layer on top of PTAA, contributed to this improvement in line with our findings from the HAXPES analysis. A broader investigation into varying NiO_x thicknesses (125, 185, 250 ALD cycles) on top of PTAA revealed that the 185 ALD cycles NiO_x layer consistently offered the best performance across multiple devices (see SI, Fig. S13). In contrast, thinner (125 ALD cycles) and thicker (250 ALD cycles) NiO_x layers led to increased performance variability and occasional shunting, likely due to incomplete coverage or increased series resistance, respectively. Detailed device statistics are provided in Section 8 of the SI.

We conclude the device study by an assessment of device stability under operational conditions, as PSCs are prone to degradation when exposed to constant illumination (see SI, Fig. S15). Previously, we discussed that compact ALD layers may be able to reduce ion migration and can enhance the photostability of PSCs. In this study, the PTAA/NiO_x device was compared with a reference PTAA device in an indoor accelerated aging test for 45 hours under an LED solar simulator with a spectrum that matched AM 1.5G in a climate chamber kept under a N_2 atmosphere at a temperature of 25 °C. The maximum power point tracking (MPPT) was conducted throughout the aging process, and J-V curves were recorded every 20 minutes. The reference PTAA device exhibited a steep decline in power (P_{MAX}) during the first 2 h, resulting in a PCE reduction to roughly 60% of its initial value (see SI, Fig. S15(a)). This decrease in efficiency can be attributed to a substantial drop in the V_{MPP} of the device, as shown in SI, Fig. S15(b), which may be attributed to an increase in trap states resulting from ion migration through the PTAA pinholes.[47] The increase in trap states leads to increased non-radiative recombination, causing a significant decline in photo-voltage, ultimately affecting the PCE.[66,67] The PTAA/NiO_x bi-layer HTL device retained 70% of its initial PCE for 45 hours with stable J_{MPP} and V_{MPP}. We ascribe the improved operational stability of this device to the compact nature of the ALD oxide, which reduces ion migration, limiting the formation of trap states. In summary, the inclusion of PTTA/ALD-NiO_x bilayer in the n-i-p architecture significantly improved device performance and operational stability due to the superior thin-film properties of ALD-NiO_x.

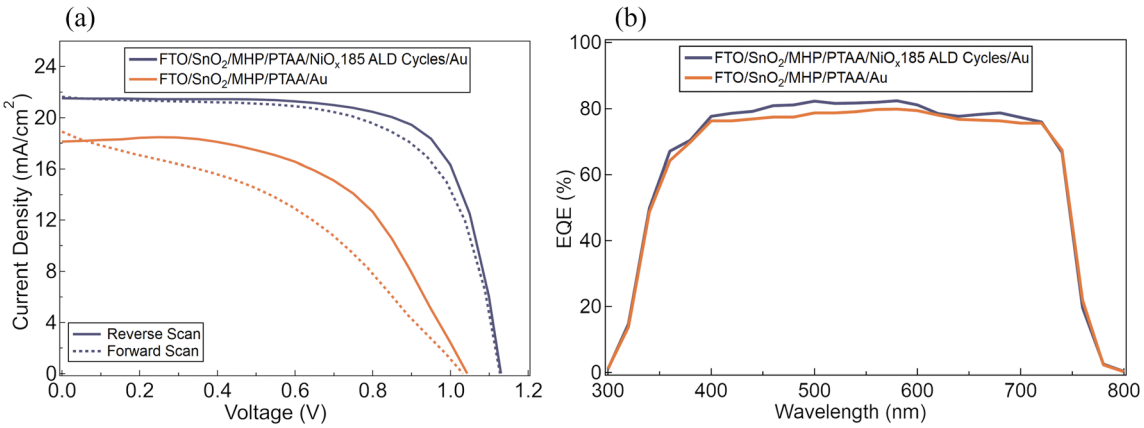

Fig. 5 (a) *J*–*V* characteristics (forward scan shown in solid line and reverse scan shown in dotted line) and (b) external quantum efficiency (EQE) of n-i-p PSCs with and without a 185 ALD cycle NiO_x overlayer.

To further understand the device performance behavior, we conducted optoelectronic studies, using hyperspectral photoluminescence (PL) imaging measurements with an excitation wavelength of 750 nm, on various sub-cell structures (FTO/SnO_2/MHP, FTO/SnO_2/MHP/NiO_x185 ALD cycles, FTO/SnO_2/MHP/PTAA, and FTO/SnO_2/MHP/PTAA/NiO_x 185 ALD cycles). For these measurements, MHP films with a stoichiometry of $FA_{0.83}Cs_{0.17}Pb(I_{0.83}Br_{0.17})_3$ were utilized, representing a slightly adjusted composition within the same mixed-cation mixed-halide system as the $FA_{0.7}Cs_{0.3}Pb(I_{0.9}Br_{0.1})_3$ used for device fabrication, and thus remains highly representative of the material system under investigation.

The PL intensity remained largely unchanged upon NiO_x deposition on MHP (FTO/SnO_2/MHP/NiO_x) relative to the pristine MHP reference, indicative of limited hole extraction efficiency of the NiO_x layer (see Fig. 6). This inefficiency likely stems from two key factors: interfacial chemical defects (such as nitrogen-containing species and iodine deficiency) that may introduce trap states, and a substantial concentration of $Ni(OH)_2$/NiOOH species in the ALD-NiO_x,[68,69] both of which could significantly hinder efficient hole transport. Conversely, samples incorporating PTAA (FTO/SnO_2/MHP/PTAA and FTO/SnO_2/MHP/PTAA/NiO_x) exhibited pronounced PL quenching relative to the MHP reference, indicative of significantly improved hole transport and extraction. The marked PL quenching in the PTAA/NiO_x sample suggests enhanced hole extraction through NiO_x when deposited atop PTAA, corroborated by previously presented HAXPES analysis revealing a reduced concentration of $Ni(OH)_2$/NiOOH species and an absence of detectable interfacial chemical defects at this interface. Moreover, as discussed earlier, the device performance of the PTAA/NiO_x-based architecture, with a champion cell

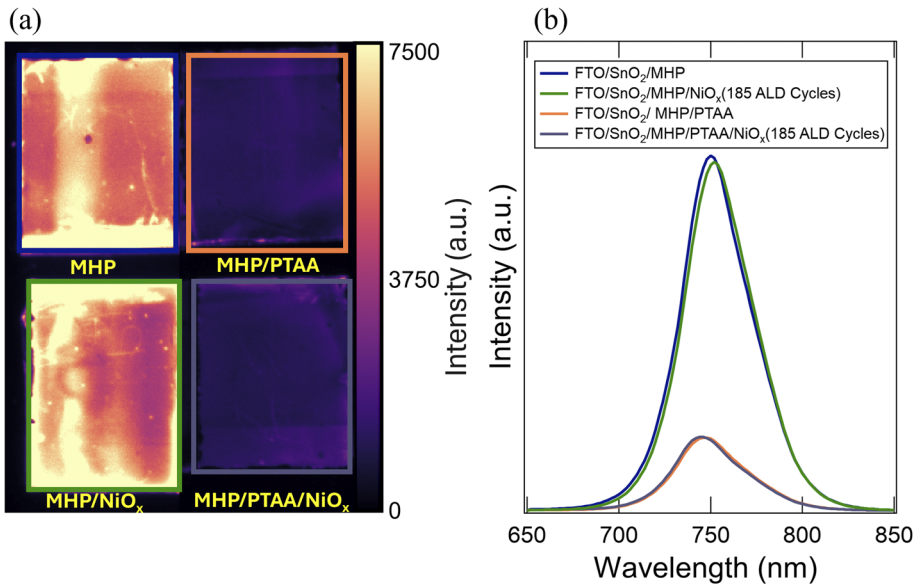

Fig. 6 (a) Hyperspectral photoluminescence (PL) images at 750 nm for FTO/SnO_2/$FA_{0.83}Cs_{0.17}Pb(I_{0.83}Br_{0.17})_3$ MHP, FTO/SnO_2/MHP/NiO_x, FTO/SnO_2/MHP/PTAA, FTO/SnO_2/MHP/PTAA/NiO_x, (b) average PL intensity.

efficiency of 17.5%, supports the effective charge transport indicated by the observed PL quenching and the interface quality revealed by HAXPES. It is noteworthy that any interfacial nonradiative recombination arising from defects at the MHP/NiO_x interface is largely masked by the dominant bulk radiative recombination in these relatively thick (~500 nm) MHP films, which governs the overall PL response.

Moving towards these advanced and ultimately more stable designs necessitates addressing the inherent limitations of conventional organic hole transport layers like PTAA. While effective in minimizing interface degradation in this study, challenges such as pinhole formation and limited chemical inertness in such layers preclude complete mitigation of unwanted reactions between MHP and ALD metal oxide precursors. Therefore, exploring alternative robust interlayers, such as two-dimensional transition metal dichalcogenides (2D TMDs), is highly promising and opens new avenues. These 2D TMDs offer superior barrier properties and chemical stability[70] for the critical interface between the MHP and the ALD metal oxide, potentially enabling complete and sustained mitigation of the observed chemical degradation, thereby pushing device longevity to new levels.

3. Conclusion

In summary, our study focused on n-i-p configuration perovskite solar cells using an ALD-NiO_x hole-transport interlayer. We conducted an extensive analysis of the interface, solar cell characteristics, and operational stability. We employed synchrotron-based HAXPES measurements to investigate the interface chemistry of MHP and ALD-NiO_x. The HAXPES study used photon energies of 2 keV and 6 keV to probe different depths of the interface. The characterization revealed crucial insights into the emergence of new chemical defects, particularly nitrogen- and lead-based compounds, at the interface. Furthermore, for the MHP/NiO_x sample we found the MHP to be significantly iodine- and nitrogen-deficient. The new interfacial species (N and Pb based chemical compound) and severe iodine and nitrogen loss of the MHP film imply the formation of several defects at the interface, originating from the chemical interaction between the MHP and ALD-NiO_x precursors. We also found that the ALD-NiO_x grown directly on MHP exhibited a low concentration of NiO (56%) in the proximity of the interface and a high concentration of hydroxide/oxy-hydroxide species. The high concentrations of hydroxide/oxy-hydroxide species are detrimental to the stability of MHP, as they can react rapidly with MHP, causing rapid degradation.

The work was also extended to a system with a 20 nm PTAA interlayer between the MHP and ALD-NiO_x. The PTAA interlayer was found to limit the MHP from interacting with the ALD-NiO_x precursors. The ALD-NiO_x films on PTAA had a higher concentration of NiO in the range of 74% and a higher work function of 4.5 eV. Upon incorporation of the PTAA/NiO_x in the n-i-p architecture PSCs, a champion cell PCE of 17.5% was recorded with a significant enhancement of operational stability under nitrogen atmosphere with respect to the PTAA HTL-based device.

Author contributions

Nitin Mallik: conceptualization, data curation, formal analysis, investigation, methodology, visualization, writing – original draft, writing – review & editing. Javid Hajhemati: data curation, investigation, visualization, methodology, writing – review & editing. Vincent Dufoulon: data curation, investigation, visualization, methodology, writing– review & editing. Damien Coutancier: investigation, writing – review & editing. Elif Hüsam: data curation, investigation, writing – review & editing. Davide Regaldo: data curation, investigation, writing – review & editing. Iwan Zimmermann: investigation, writing – review & editing. Karim Medjoubi: investigation, writing – review & editing. Michael A. Anderson: data curation, investigation, writing – review & editing. Damien Aureau: investigation, writing – review & editing. Mathieu Frégnaux: investigation, writing – review & editing. Roberto Félix: investigation, methodology, supervision, writing – review & editing, data curation, formal analysis. Regan G. Wilks: data curation, formal analysis, investigation, methodology, project administration, supervision, validation, writing – review & editing. Nathanaelle Schneider: conceptualization, methodology, resources, supervision, validation, writing – review & editing. Marcus Bär: conceptualization, formal analysis, funding acquisition, methodology, project administration, resources, supervision, validation, writing – review & editing. Philip Schulz: conceptualization, data curation, formal analysis, funding acquisition, methodology, project administration, resources, supervision, validation, visualization, writing – review & editing.

Conflicts of interest

The authors declare no competing financial interest.

Data availability

The IMFP values calculated using NIST SESSA software (available at **https://www.nist.gov/publications/nist-database-simulation-electron-spectra-surface-analysis-sessa-version-211**) are included as part of the SI. Supplementary information: Experimental methods; structural and morphological properties of perovskite, PTAA, and ALD-NiO_x; XPS and HAXPES data and graphs, n-i-p solar cell statistics and operational stability. See DOI: **https://doi.org/10.1039/d5el00044k**.

Acknowledgements

This work was financially supported by the French Agence Nationale de la Recherche (ANR) with grant number: ANR-17-MPGA0012 and IPVF ANR-IEED-002-01. Furthermore, the work was funded by the ANR and the DFG *via* the bilateral research project ALSATIAN with the grant number ANR-23-CE50-0030. We thank Alexandre Blaizot for the SEM images. We thank HZB for the allocation of synchrotron radiation beamtime at BESSY II for HAXPES measurements and the Energy Materials *In situ* Laboratory Berlin (EMIL) for providing infrastructure allowing sample handling and mounting in inert gas

atmosphere. MAA acknowledges support from the Fully Connected Virtual and Physical Perovskite Photovoltaic Lab (VIPERLAB) project.

References

1 NREL efficiency chart, can be found under **https://www.nrel.gov/pv/cell-efficiency**.
2 E. Aydin, T. G. Allen, M. De Bastiani, A. Razzaq, L. Xu, E. Ugur, J. Liu and S. De Wolf, *Science*, 2024, **383**, eadh3849, DOI: **10.1126/science.adh3849**.
3 J. Zhou, L. Tan, Y. Liu, H. Li, X. Liu, M. Li, S. Wang, Y. Zhang, C. Jiang, R. Hua, W. Tress, S. Meloni and C. Yi, *Joule*, 2024, **8**(6), 1691–1706, DOI: **10.1016/j.joule.2024.02.019**.
4 M. He, K. Sun and X. Hao, Electronic and Optical Properties of Perovskite Semiconductor, *Perovskite Optoelectronic Devices*, ed. B. Pradhan, Engineering Materials, Springer, Cham, 2024, pp. 51–70, DOI: **10.1007/978-3-031-57663-8_3**.
5 F. Zhang, D. Zheng, D. Yu, S. Wu, K. Wang, L. Peng, S. (Frank) Liu and D. Yang, *Nano Energy*, 2024, **124**, 109503, DOI: **10.1016/j.nanoen.2024.109503**.
6 Y. Li, Y. Wang, Z. Xu, B. Peng and X. Li, *ACS Nano*, 2024, **18**, 10688.
7 P. Schulz, D. Cahen and A. Kahn, *Chem. Rev.*, 2019, **119**, 3349–3417, DOI: **10.1021/acs.chemrev.8b00558**.
8 P. Schulz, *ACS Energy Lett.*, 2018, **3**, 1287–1293, DOI: **10.1021/acsenergylett.8b00404**.
9 J. A. Christians, P. Schulz, J. S. Tinkham, T. H. Schloemer, S. P. Harvey, B. J. Tremolet De Villers, A. Sellinger, J. J. Berry and J. M. Luther, *Nat. Energy*, 2018, **3**, 68.
10 J. Xia, M. Sohail and M. K. Nazeeruddin, *Adv. Mater.*, 2023, **35**, 2211324, DOI: **10.1002/adma.202211324**.
11 Deepika, A. Singh, U. K. Verma and A. Tonk, *Phys. Status Solidi A*, 2023, **220**, 2200736, DOI: **10.1002/pssa.202200736**.
12 T. Wang, W. Deng, J. Cao and F. Yan, *Adv. Energy Mater.*, 2023, **13**, 2201436, DOI: **10.1002/aenm.202201436**.
13 F. M. Rombach, S. A. Haque and T. J. Macdonald, *Energy Environ. Sci.*, 2021, **14**, 5161–5190, DOI: **10.1039/d1ee02095a**.
14 Y. Ko, Y. Kim, C. Lee, Y. Kim and Y. Jun, *ACS Appl. Mater. Interfaces*, 2018, **10**, 11633–11641, DOI: **10.1021/acsami.7b18745**.
15 E. J. Juarez-Perez, M. R. Leyden, S. Wang, L. K. Ono, Z. Hawash and Y. Qi, *Chem. Mater.*, 2016, **28**, 5702–5709, DOI: **10.1021/acs.chemmater.6b01777**.
16 K. M. Anoop and T. N. Ahipa, *Sol. Energy*, 2023, **263**, 111937, DOI: **10.1016/j.solener.2023.111937**.
17 Z. Li, C. Xiao, Y. Yang, S. P. Harvey, D. H. Kim, J. A. Christians, M. Yang, P. Schulz, S. U. Nanayakkara, C. S. Jiang, J. M. Luther, J. J. Berry, M. C. Beard, M. M. Al-Jassim and K. Zhu, *Energy Environ. Sci.*, 2017, **10**, 1234–1242, DOI: **10.1039/c7ee00358g**.
18 C. Zhang, K. Wei, J. Hu, X. Cai, G. Du, J. Deng, Z. Luo, X. Zhang, Y. Wang, L. Yang and J. Zhang, *Mater. Today*, 2023, **67**, 518–547, DOI: **10.1016/j.mattod.2023.06.009**.
19 R. Wang, X. Dong and Y. Liu, *Chin. J. Chem.*, 2023, **41**(23), 3373–3387, DOI: **10.1002/cjoc.202300252**.
20 H. Park, P. Nandi, Y. In and H. Shin, *Sol. RRL*, 2024, **8**(4), 2300858, DOI: **10.1002/solr.202300858**.
21 K. C. Wang, J. Y. Jeng, P. S. Shen, Y. C. Chang, E. W. G. Diau, C. H. Tsai, T. Y. Chao, H. C. Hsu, P. Y. Lin, P. Chen, T. F. Guo and T. C. Wen, *Sci. Rep.*, 2014, **4**, 4756, DOI: **10.1038/srep04756**.
22 M. Li, H. Li, Q. Zhuang, D. He, B. Liu, C. Chen, B. Zhang, T. Pauporté, Z. Zang and J. Chen, *Angew. Chem., Int. Ed.*, 2022, **61**(35), e202206914, DOI: **10.1002/anie.202206914**.
23 V. Zardetto, B. L. Williams, A. Perrotta, F. Di Giacomo, M. A. Verheijen, R. Andriessen, W. M. M. Kessels and M. Creatore, *Sustainable Energy Fuels*, 2017, **1**, 30.
24 Z. Xing, J. Xiao, T. Hu, X. Meng, D. Li, X. Hu and Y. Chen, *Small Methods*, 2020, **4**, 1.
25 A. Hultqvist, T. J. Jacobsson, S. Svanström, M. Edoff, U. B. Cappel, H. Rensmo, E. M. J. Johansson, G. Boschloo and T. Törndahl, *ACS Appl. Energy Mater.*, 2021, **4**, 510.
26 A. E. A. Bracesco, C. H. Burgess, A. Todinova, V. Zardetto, D. Koushik, W. M. M. (Erwin) Kessels, I. Dogan, C. H. L. Weijtens, S. Veenstra, R. Andriessen and M. Creatore, *J. Vac. Sci. Technol., A*, 2020, **38**, 063206.
27 A. E. A. Bracesco, J. W. P. Jansen, H. Xue, V. Zardetto, G. Brocks, W. M. M. Kessels, S. Tao and M. Creatore, *ACS Appl. Mater. Interfaces*, 2023, **15**(31), 38018–38028, DOI: **10.1021/acsami.3c05647**.
28 N. Mallik, J. Hajhemati, M. Frégnaux, D. Coutancier, A. Toby, S.-T. Zhang, C. Hartmann, E. Hüsam, A. Saleh, T. Vincent, O. Fournier, R. G. Wilks, D. Aureau, R. Félix, N. Schneider, M. Bär and P. Schulz, *Nano Energy*, 2024, **126**, 109582.
29 S. A. Johnson, K. P. White, J. Tong, S. You, A. Magomedov, B. W. Larson, D. Morales, R. Bramante, E. Dunphy, R. Tirawat, C. L. Perkins, J. Werner, G. Lahti, C. Velez, M. F. Toney, K. Zhu, M. D. McGehee, J. J. Berry and A. F. Palmstrom, *Joule*, 2023, **7**(12), 2873–2893, DOI: **10.1016/j.joule.2023.10.009**.
30 M. Kedia, C. Das, M. Kot, Y. Yalcinkaya, W. Zuo, K. Tabah Tanko, P. Matvija, M. Ezquer, I. Cornago, W. Hempel, F. Kauffmann, P. Plate, M. Lira-Cantu, S. A. L. Weber and M. Saliba, *Energy Environ. Sci.*, 2025, **18**, 5250–5263, DOI: **10.1039/d4ee05703a**.
31 I. S. Kim and A. B. F. Martinson, *J. Mater. Chem. A*, 2015, **3**, 20092–20096, DOI: **10.1039/c5ta07186k**.
32 C. Zheng and O. Rubel, *J. Phys. Chem. C*, 2019, **123**(32), 19385–19394, DOI: **10.1021/acs.jpcc.9b05516**.
33 Z. Li, M. Yang, J. S. Park, S. H. Wei, J. J. Berry and K. Zhu, *Chem. Mater.*, 2016, **28**(1), 284–292, DOI: **10.1021/acs.chemmater.5b04107**.
34 C. Yi, J. Luo, S. Meloni, A. Boziki, N. Ashari-Astani, C. Grätzel, S. M. Zakeeruddin, U. Röthlisberger and M. Grätzel, *Energy Environ. Sci.*, 2016, **9**, 656–662, DOI: **10.1039/c5ee03255e**.
35 J. W. Lee, D. H. Kim, H. S. Kim, S. W. Seo, S. M. Cho and N. G. Park, *Adv. Energy Mater.*, 2015, **5**, 1501310, DOI: **10.1002/aenm.201501310**.
36 J. Kim, K. S. Kim and C. W. Myung, *npj Comput. Mater.*, 2020, **6**, 1.
37 A. Hultqvist, K. Aitola, K. Sveinbjörnsson, Z. Saki, F. Larsson, T. Törndahl, E. Johansson, G. Boschloo and M. Edoff, *ACS*

Appl. Mater. Interfaces, 2017, **9**(35), 29707–29716, DOI: 10.1021/acsami.7b07627.

38 A. F. Palmstrom, J. A. Raiford, R. Prasanna, K. A. Bush, M. Sponseller, R. Cheacharoen, M. C. Minichetti, D. S. Bergsman, T. Leijtens, H. P. Wang, V. Bulović, M. D. McGehee and S. F. Bent, *Adv. Energy Mater.*, 2018, **8**, 1.

39 A. Hultqvist, T. J. Jacobsson, S. Svanström, M. Edoff, U. B. Cappel, H. Rensmo, E. M. J. Johansson, G. Boschloo and T. Törndahl, *ACS Appl. Energy Mater.*, 2021, **4**, 510.

40 C. C. Boyd, R. Cheacharoen, T. Leijtens and M. D. McGehee, *Chem. Rev.*, 2019, **119**, 3418–3451, DOI: 10.1021/acs.chemrev.8b00336.

41 X. Yan, W. Fan, F. Cheng, H. Sun, C. Xu, L. Wang, Z. Kang and Y. Zhang, *Nano Today*, 2022, **44**, 101503, DOI: 10.1016/j.nantod.2022.101503.

42 S. R. Pering and P. J. Cameron, *Mater. Adv.*, 2022, **3**, 7918–7924, DOI: 10.1039/d2ma00619g.

43 E. M. Hutter, L. A. Muscarella, F. Wittmann, J. Versluis, L. McGovern, H. J. Bakker, Y. W. Woo, Y. K. Jung, A. Walsh and B. Ehrler, *Cell Rep. Phys. Sci.*, 2020, **1**(8), 100120, DOI: 10.1016/j.xcrp.2020.100120.

44 M. Gorgoi, S. Svensson, F. Schäfers, G. Öhrwall, M. Mertin, P. Bressler, O. Karis, H. Siegbahn, A. Sandell, H. Rensmo, W. Doherty, C. Jung, W. Braun and W. Eberhardt, *Nucl. Instrum. Methods Phys. Res., Sect. A*, 2009, **601**(1–2), 48–53, DOI: 10.1016/j.nima.2008.12.244.

45 F. Schaefers, M. Mertin and M. Gorgoi, *Rev. Sci. Instrum.*, 2007, **78**, 123102, DOI: 10.1063/1.2808334.

46 H. Dong, C. Zhang, W. Nie, S. Duan, C. N. Saggau, M. Tang, M. Zhu, Y. S. Zhao, L. Ma and O. G. Schmidt, *Angew. Chem., Int. Ed.*, 2022, **61**(13), e202115875, DOI: 10.1002/anie.202115875.

47 C. M. Wolff, P. Caprioglio, M. Stolterfoht and D. Neher, *Adv. Mater.*, 2019, **31**, 1902762, DOI: 10.1002/adma.201902762.

48 M. Ayiania, M. Smith, A. J. R. Hensley, L. Scudiero, J. S. McEwen and M. Garcia-Perez, *Carbon*, 2020, **162**, 528–544, DOI: 10.1016/j.carbon.2020.02.065.

49 A. M. López-Vinasco, L. M. Martínez-Prieto, J. M. Asensio, P. Lecante, B. Chaudret, J. Cámpora and P. W. N. M. Van Leeuwen, *Catal. Sci. Technol.*, 2020, **10**, 342–350, DOI: 10.1039/c9cy02172h.

50 C. C. Boyd, R. C. Shallcross, T. Moot, R. Kerner, L. Bertoluzzi, A. Onno, S. Kavadiya, C. Chosy, E. J. Wolf, J. Werner, J. A. Raiford, C. de Paula, A. F. Palmstrom, Z. J. Yu, J. J. Berry, S. F. Bent, Z. C. Holman, J. M. Luther, E. L. Ratcliff, N. R. Armstrong and M. D. McGehee, *Joule*, 2020, **4**, 1759–1775, DOI: 10.1016/j.joule.2020.06.004.

51 M. C. Biesinger, B. P. Payne, L. W. M. Lau, A. Gerson and R. S. C. Smart, *Surf. Interface Anal.*, 2009, **41**, 324–332, DOI: 10.1002/sia.3026.

52 A. P. Grosvenor, M. C. Biesinger, R. S. C. Smart and N. S. McIntyre, *Surf. Sci.*, 2006, **600**, 4170–4175, DOI: 10.1016/j.susc.2006.01.041.

53 A. N. Mansour, *Surf. Sci. Spectra*, 1994, **3**, 231–238, DOI: 10.1116/1.1247751.

54 A. N. Mansour, *Surf. Sci. Spectra*, 1994, **3**, 239–246, DOI: 10.1116/1.1247752.

55 A. N. Mansour and C. A. Melendres, *Surf. Sci. Spectra*, 1994, **3**, 271–278, DOI: 10.1116/1.1247756.

56 A. N. Mansour and C. A. Melendres, *Surf. Sci. Spectra*, 1994, **3**, 255–262, DOI: 10.1116/1.1247754.

57 M. W. Roberts and R. S. C. Smart, *J. Chem. Soc., Faraday Trans. 1 F*, 1984, **80**, 2957–2968, DOI: 10.1039/F19848002957.

58 A. F. Carley, P. R. Chalker and M. W. Roberts, *Proc. R. Soc. London, Ser. A*, 1985, **399**(1816), 167–179, DOI: 10.1098/rspa.1985.0053.

59 M. C. Biesinger, *Appl. Surf. Sci.*, 2022, **597**, 153681, DOI: 10.1016/j.apsusc.2022.153681.

60 R. P. Gupta and S. K. Sen, *Phys. Rev. B*, 1974, **10**, 71, DOI: 10.1103/PhysRevB.10.71.

61 R. P. Gupta and S. K. Sen, *Phys. Rev. B*, 1975, **12**, 15, DOI: 10.1103/PhysRevB.12.15.

62 G. H. Major, N. Fairley, P. M. A. Sherwood, M. R. Linford, J. Terry, V. Fernandez and K. Artyushkova, *J. Vac. Sci. Technol., A*, 2020, **38**, 061203, DOI: 10.1116/6.0000377.

63 M. T. Greiner, M. G. Helander, Z. Bin Wang, W. M. Tang and Z. H. Lu, *J. Phys. Chem. C*, 2010, **114**, 19777–19781, DOI: 10.1021/jp108281m.

64 T. Leijtens, G. E. Eperon, N. K. Noel, S. N. Habisreutinger, A. Petrozza and H. J. Snaith, *Adv. Energy Mater.*, 2015, **5**, 1500963, DOI: 10.1002/aenm.201500963.

65 H. J. Snaith, A. Abate, J. M. Ball, G. E. Eperon, T. Leijtens, N. K. Noel, S. D. Stranks, J. T. W. Wang, K. Wojciechowski and W. Zhang, *J. Phys. Chem. Lett.*, 2014, **5**, 1511–1515, DOI: 10.1021/jz500113x.

66 M. Stolterfoht, P. Caprioglio, C. M. Wolff, J. A. Márquez, J. Nordmann, S. Zhang, D. Rothhardt, U. Hörmann, Y. Amir, A. Redinger, L. Kegelmann, F. Zu, S. Albrecht, N. Koch, T. Kirchartz, M. Saliba, T. Unold and D. Neher, *Energy Environ. Sci.*, 2019, **12**, 2778–2788, DOI: 10.1039/c9ee02020a.

67 I. Gelmetti, N. F. Montcada, A. Pérez-Rodríguez, E. Barrena, C. Ocal, I. García-Benito, A. Molina-Ontoria, N. Martín, A. Vidal-Ferran and E. Palomares, *Energy Environ. Sci.*, 2019, **12**, 1309–1316, DOI: 10.1039/c9ee00528e.

68 N. Tiwari, H. Arianita Dewi, E. Erdenebileg, R. Narayan Chauhan, N. Mathews, S. Mhaisalkar and A. Bruno, *Sol. RRL*, 2022, **6**, 2270032.

69 D. Yuk, J. Roe, Y. Lee, J. Kim, J. Seo, J. Yeop, T. Song and J. Y. Kim, *ACS Appl. Energy Mater.*, 2024, **7**, 4558.

70 B. Kim, M. Kim, H. Kim, S. Jeong, J. Yang and M. S. Jeong, *ACS Appl. Mater. Interfaces*, 2022, **14**(31), 35726–35733, DOI: 10.1021/acsami.2c08680.